

Numerical modeling of wing crack propagation accounting for fracture contact mechanics

Hau Trung Dang, Eirik Keilegavlen, Inga Berre.

Department of Mathematics, University of Bergen, Bergen, Norway

Keywords: fracture propagation; wing crack development; shear slip; adaptive remeshing; linear elastic fracture mechanics; contact mechanics.

ABSTRACT

As a consequence of shearing, wing cracks can emerge from pre-existing fractures. The process involves the interaction of sliding of the existing fracture surfaces and the tensile material failure that creates wing cracks. This work devises a numerical model to investigate how wing cracks emerge, propagate and connect pre-existing fractures under shear processes. A mathematical and numerical model for wing crack propagation based on linear elastic fracture mechanics that also accounts for fracture contact mechanics is presented. Computational efficiency is ensured by an adaptive remeshing technique. The numerical model is verified and validated through a comparison of the analytical and experimental results. Additional numerical examples illustrate the performance of the method for complex test cases where wing-cracks develop for multiple pre-existing and interacting fractures.

1. Introduction

Wing cracks can develop from a pre-existing fracture when the fracture is subjected to shear processes. This occurs for many applications where fractured media are subjected to anisotropic stress regimes. For example, in fractured subsurface systems, fractures will slip if shear forces overcome the cohesion and frictional strength of the contact between the fracture surfaces. This can occur due to natural changes in tectonic stresses, but the process can also be induced by fluid injection, such as in situations of geothermal reservoirs. In the latter case, elevated pressures reduce the effective normal stress on the fracture, ultimately causing slip if the reduction in the normal stress is sufficient for the shear forces to overcome the cohesion and frictional resistance of the fracture. The slip of the fracture surfaces in opposite directions can cause the fracture to propagate in the form of wing cracks, possibly creating enhanced reservoir connectivity (Cheng et al., 2019; Jung, 2013; McClure and Horne, 2014; Norbeck et al., 2018). Understanding this mechanism is, thus, crucial in the simulation of fractured subsurface formations.

Many experimental studies have been published that consider the formation, growth and connection of wing cracks caused by external compressive loading in specimens made of rock or rock-like materials (Haeri et al., 2014a, 2014b; Horii and Nemat-Nasser, 1985; Ingraffea and Manu, 1980). In these experiments, if the pre-existing fracture is not perpendicular to the external load, wing cracks emerge at the tip and tend to align with the direction of the maximum compressive stress. The same conclusion is drawn from mathematical modeling. Based on the finite element method (FEM), Ingraffea and Heuze (Ingraffea and Heuze, 1980) predicted the propagation of wing cracks in rock structures by using all three stress, energy and strain criteria. Primary crack trajectories predicted by the stress and energy criteria are in good agreement with the observed trajectories. Based on the phase-field model (Bryant and Sun, 2018) and a modified phase-field model (Zhang et al., 2017), wing crack propagation was modeled using energy criteria that divided the active energy density into distinct parts corresponding to different crack modes (mode I and mode II). Sharafisafa and Nazem (Sharafisafa and Nazem, 2014) used the vector level set with both the discrete element method and the extended finite element method (XFEM) to model the wing crack propagation and coalescence in fractured rock masses. It was recognized that using the FEM with stress criteria (the maximum tangential stress - MTS) seems to be the best choice for wing crack modeling because of the simplification and agreement with the observed trajectories (Gonçalves da Silva and Einstein, 2013; Ingraffea and Heuze, 1980).

While wing cracks develop as tensile fractures, the pre-existing fractures that wing cracks emerge from may be either open or in contact. This necessitates the inclusion of fracture contact mechanics in the wing crack models (Oden and Pires, 1983; Ueber et al., 2008). There are several ways to formulate the contact mechanics corresponding to the different types of discretization. For example, based on the semianalytical displacement discontinuity method, Kamali and Ghassemi (Kamali and Ghassemi, 2018) developed a simulation model in which the closed natural fractures were represented by so-called contact displacement discontinuity elements (Asgian, 1988), approximating the contact mechanics condition. However, the approach has limitations in dealing with the interaction between multiple fractures due to inherent limitations of the semianalytical displacement discontinuity method.

In FEM, equilibrium of linear elasticity is described as a displacement field minimizes the potential energy. Then, the contact should be considered as an inequality constraint of the optimization formulation. This means that the potential energy is minimized while satisfying a contact constraint assumed to be a nonpenetration condition between the surfaces of the

fracture. The inequality constraint can be solved by some methods, such as the active-set, Frank-Wolfe, penalty or barrier methods (Hüeber and Wohlmuth, 2005; Ueber et al., 2008).

An inherent problem in the simulation of fracture propagation is the disparate length scales. While the simulation domain can be quite large, the fracturing processes occur on a scale that is several orders of magnitude smaller. Moreover, most numerical methods for fracture propagation are dependent on resolving the fracture in a grid; however, the fracture path is not known a priori. A possible remedy for both of these issues is to apply adaptive remeshing (ARM) techniques to refine and adjust the mesh around an advancing fracture path.

This paper presents a mathematical model and corresponding numerical solution approach to simulate the development of wing cracks while accounting for fracture contact mechanics. First, in Section 2, the mathematical model for wing crack propagation is formulated based on the linear elasticity theory, in combination with the criteria for fracture propagation. Fracture surfaces are allowed to be in contact or fully open, modeled by contact mechanics. Section 3 presents the numerical solution approach. The governing equations are discretized using a finite element method with collapsed quarter-point elements at the fracture tips. This is combined with an adaptive remeshing technique based on error estimates and Laplacian smoothing. The contact mechanics are implemented by using an active set method. Section 4 presents several numerical test cases. The obtained results are compared with both the analytical and experimental data to verify, validate and show the accuracy of the proposed model and procedure. Finally, more complex test cases where wing cracks develop for multiple pre-existing and interacting fractures show the capability of the proposed approach in modeling the development of wing cracks under shear processes.

2. Governing equations

A mathematical model for wing crack propagation based on linear elastic fracture mechanics is presented in the following section. Emphasis is placed on the conditions on the boundaries of existing and newly formed fracture paths. We also describe the criterion used to decide when, where and how far a fracture will propagate.

2.1. Elasticity

Consider a domain $\Omega \subset \mathbb{R}^2$ with an outward unit normal vector \mathbf{n} on its boundary and a pre-existing fracture with boundaries denoted by Γ_C^\pm as shown in Fig. 1. The Dirichlet and Neumann conditions are applied on the boundary. Ignoring, for the moment, the internal

boundary conditions on the fracture, the governing equations for a linear elastic body can be expressed as

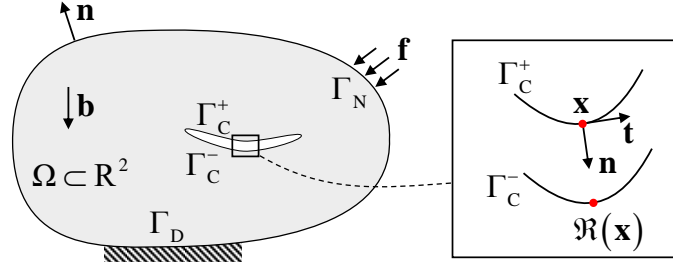


Fig. 1. An elastic body containing a pre-existing fracture.

$$\begin{cases}
 \nabla \cdot \boldsymbol{\sigma} + \mathbf{b} = 0 & \text{in } \Omega & \text{Equilibrium eq.} \\
 \boldsymbol{\sigma} = \mathbf{C} : \boldsymbol{\varepsilon} & \text{in } \Omega & \text{Constitutive eq.} \\
 \boldsymbol{\varepsilon} = \frac{1}{2}(\nabla \mathbf{u} + \nabla \mathbf{u}^T) & \text{in } \Omega & \text{Kinematic eq.} \\
 \mathbf{u} = \mathbf{u}_0 & \text{on } \Gamma_D & \text{Dirichlet BC} \\
 \boldsymbol{\sigma} \cdot \mathbf{n} = \mathbf{f} & \text{on } \Gamma_N & \text{Neumann BC}
 \end{cases} \quad (1)$$

Here, $\boldsymbol{\sigma}$, $\boldsymbol{\varepsilon}$ and $\mathbf{u} = \{u, v\}^T$ are the Cauchy stress tensor, the symmetric infinitesimal strain tensor and the displacement field, respectively; \mathbf{C} is the fourth-order elasticity (Hooke's) tensor defined by the Young's modulus, E , and Poisson's ratio, ν ; \mathbf{b} is the body force; and \mathbf{u}_0 and \mathbf{f} are the prescribed displacement along the Dirichlet boundary and the applied traction along the Neumann boundary, respectively.

To formulate the contact mechanics at the internal boundary, the fracture's boundary is divided into a positive side Γ_C^+ and a negative side Γ_C^- . Let $\mathbf{n}(\mathbf{x})$ denote the normal vector initiating from \mathbf{x} at side Γ_C^+ to side Γ_C^- . The initial gap between the two fracture sides is $g(x) \geq 0$. The jump in the normal direction of the fracture, $[\mathbf{u}(\mathbf{x})]_{\mathbf{n}}$, and the contact force in the normal direction, $\mathbf{f}_{\mathbf{n}}(\mathbf{x})$, are given by

$$[\mathbf{u}(\mathbf{x})]_{\mathbf{n}} = [\mathbf{u}(\mathbf{x})] \cdot \mathbf{n}(\mathbf{x}), \quad f_{\mathbf{n}}(\mathbf{x}) = \mathbf{f}(\mathbf{x}) \cdot \mathbf{n}(\mathbf{x}), \quad \mathbf{x} \in \Gamma_C^+ \quad (2)$$

where $\mathbf{f}(\mathbf{x}) = \boldsymbol{\sigma}(\mathbf{x}) \cdot \mathbf{n}(\mathbf{x})$ is the contact force, which vanishes in the case of an open fracture.

A nonpenetration condition is enforced in the normal direction of the fracture segments. This condition is governed by the Karush-Kuhn-Tucker (KKT) condition for the normal displacement jump and the contact force, which reads

$$\left[\mathbf{u}(\mathbf{x}) \right]_{\mathbf{n}} - g(\mathbf{x}) \leq 0, \quad \mathbf{f}_{\mathbf{n}}(\mathbf{x}) \leq 0, \quad \mathbf{f}_{\mathbf{n}}(\mathbf{x}) \left(\left[\mathbf{u}(\mathbf{x}) \right]_{\mathbf{n}} - g(\mathbf{x}) \right) = 0, \quad \mathbf{x} \in \Gamma_{\mathbf{C}}^+ \quad (3)$$

If $\Gamma_{\mathbf{C}}^+$ and $\Gamma_{\mathbf{C}}^-$ are in contact, by Newton's third law, the contact forces on both sides are equal but in opposite directions; that is

$$\mathbf{f}(\mathbf{x}) = -\mathbf{f}(\mathfrak{R}(\mathbf{x})), \quad \mathbf{x} \in \Gamma_{\mathbf{C}}^+ \quad (4)$$

in which $\mathfrak{R}: \Gamma_{\mathbf{C}}^+ \rightarrow \Gamma_{\mathbf{C}}^-$ is a mapping that projects a point from side $\Gamma_{\mathbf{C}}^+$ onto side $\Gamma_{\mathbf{C}}^-$ in the normal direction. The displacement jump, $\left[\mathbf{u}(\mathbf{x}) \right]$, is then defined by

$$\left[\mathbf{u}(\mathbf{x}) \right] = \mathbf{u}(\mathbf{x}) - \mathbf{u}(\mathfrak{R}(\mathbf{x})), \quad \mathbf{x} \in \Gamma_{\mathbf{C}}^+ \quad (5)$$

For the tangential direction of $\Gamma_{\mathbf{C}}$, two types of conditions are considered: Either the fracture surfaces are modeled as frictionless, or the displacement jump in the tangential direction is specified. For frictionless fracture surfaces, the tangential traction is zero at $\Gamma_{\mathbf{C}}$; i.e.

$$\boldsymbol{\sigma}(\mathbf{x}) \cdot \mathbf{t}(\mathbf{x}) = \boldsymbol{\sigma}(\mathfrak{R}(\mathbf{x})) \cdot \mathbf{t}(\mathfrak{R}(\mathbf{x})) = 0, \quad \mathbf{x} \in \Gamma_{\mathbf{C}}^+ \quad (6)$$

where $\mathbf{t}(\mathbf{x})$ is the tangential vector initiating from \mathbf{x} at side $\Gamma_{\mathbf{C}}^+$. The assumption of zero friction leads to an exaggeration of the slip but is acceptable herein, as the trajectory of the fracture is the primary quantity of interest. For the friction-free case, the deformation of the elastic medium and the fractures contained within are driven by the body force, external boundary conditions on $\Gamma_{\mathbf{D}}$ and $\Gamma_{\mathbf{N}}$, or displacements on other fractures.

The second type of condition is a specified displacement jump in the tangential direction of the fracture, i.e.

$$\left[\mathbf{u}(\mathbf{x}) \right]_{\mathbf{t}} = \left[\mathbf{u}(\mathbf{x}) - \mathbf{u}(\mathfrak{R}(\mathbf{x})) \right] \cdot \mathbf{t}(\mathbf{x}) = u_0 \quad (7)$$

where the total slip at $\Gamma_{\mathbf{C}}$, u_0 , is considered as known. This type of condition is relevant to mimic the slip along an existing fracture, which in applications, may be triggered by effects not considered in the present model.

The wing cracks emerging due to the shear force on existing fractures are tensile cracks (Bobet and Einstein, 1998; Wong and Einstein, 2009). This means that their surfaces are in not

contact and both normal and tangential tractions at the corresponding fracture faces are zero; i.e.

$$\boldsymbol{\sigma} \cdot \mathbf{n} = \boldsymbol{\sigma} \cdot \mathbf{t} = 0 \quad (8)$$

The wing cracks are not present in the computational domain at the start of the simulations. Indeed, the computation of the point of failure and the paths of the wing crack that develop are the main challenges that are addressed in this work.

2.2. Failure and propagation

The wing crack growth processes are governed by a fracture criterion. From the mathematical model for elastic deformation, the stress at an arbitrary point can be directly calculated for a certain problem. In this work, we chose to adapt the fracture criterion based on the maximum tangential stress (MTS) (Erdogan and Sih, 1963), which is simple and sufficiently accurate (Gonçalves da Silva and Einstein, 2013; Ingraffea and Heuze, 1980), to predict the initiation and propagation angle of wing cracks. This criterion states that a crack grows when the maximum average tangential stress in the fracture process zone ahead of the crack tip reaches a critical value. Moreover, the crack growth direction coincides with the direction of the maximum average tangential stress along a constant radius around the crack tip. In polar coordinates (r, θ) with the origin at the crack tip, the tangential stress has the following form (Erdogan and Sih, 1963)

$$\sigma_{\theta}(r, \theta) = \frac{1}{\sqrt{2\pi r}} \left(K_{\text{I}} \cos^3 \frac{\theta}{2} - \frac{3}{2} K_{\text{II}} \cos \frac{\theta}{2} \sin \theta \right) \quad (9)$$

where r is the distance from the tip. K_{I} and K_{II} are the stress intensity factors (SIFs), which are measures for the intensity of stresses close to the crack tip. The wing crack emerges if the tangential stress reaches a critical value, i.e.,

$$\sigma_{\theta_0} \sqrt{2\pi r} = K_{\text{I}} \cos^3 \frac{\theta_0}{2} - \frac{3}{2} K_{\text{II}} \cos \frac{\theta_0}{2} \sin \theta_0 = K_{\text{IC}} \quad (10)$$

where K_{IC} is the material toughness and θ_0 is the crack initiation angle with respect to the original crack plane. θ_0 is obtained by solving $\partial \sigma_{\theta} / \partial \theta = 0$ for θ and combining the result with the sufficient condition $\partial^2 \sigma_{\theta} / \partial \theta^2 < 0$ such that

$$\theta_0 = 2 \tan^{-1} \left(\frac{1}{4} \mu \pm \frac{1}{4} \sqrt{\mu^2 + 8} \right), \quad \mu = K_{\text{I}} / K_{\text{II}} \quad (11)$$

$$K_{II} \left(\sin \frac{\theta_0}{2} + 9 \sin \frac{3\theta_0}{2} \right) < K_I \left(\cos \frac{\theta_0}{2} + 3 \cos \frac{3\theta_0}{2} \right) \quad (12)$$

When the wing crack emerges, i.e., the criterion shown in Eq. (10) is satisfied, the increment of each fracture needs to be determined. For a single crack propagation, the increment is defined by a fixed distance such as the crack tip rosette radius h . In the case where more than one crack grows simultaneously, the tips with the highest energy in the fracture set advance significantly further than the others (Paluszny and Matthäi, 2009). The increment for each tip is defined by the Paris-type law (Paris and Erdogan, 1963; Renshaw and Pollard, 1994)

$$L_{adv}^i = L_{max} \left(\frac{G_i}{\max(G_i)} \right)^\alpha \quad (13)$$

where L_{adv}^i and G_i are the propagation length and the energy release rate for the i^{th} propagation crack, respectively, L_{max} is the maximum length increase at any propagation step, and the exponent α is a numerical parameter, which is set to 0.35 in this work (Renshaw and Pollard, 1994). For a general fracture in a two-dimensional domain, the energy release around the fracture tip is given by

$$G = \frac{(1+\nu)(1+k)}{4E} (k_I^2 + k_{II}^2) \quad (14)$$

Here, k_I and k_{II} are the local mode I and mode II stress intensity factors at the tip obtained by summing the normal and shear stresses (Anderson, 2017), respectively

$$k_I = \sigma_{yy} \sqrt{2\pi h} = \frac{1}{4} \left[3 \cos \left(\frac{\theta_0}{2} \right) + \cos \left(\frac{3\theta_0}{2} \right) \right] K_I - \frac{1}{4} \left[3 \sin \left(\frac{\theta_0}{2} \right) - 3 \sin \left(\frac{3\theta_0}{2} \right) \right] K_{II} \quad (15)$$

$$k_{II} = \tau_{xy} \sqrt{2\pi h} = \frac{1}{4} \left[\sin \left(\frac{\theta_0}{2} \right) + \sin \left(\frac{3\theta_0}{2} \right) \right] K_I + \frac{1}{4} \left[\cos \left(\frac{\theta_0}{2} \right) + 3 \cos \left(\frac{3\theta_0}{2} \right) \right] K_{II} \quad (16)$$

3. Discretization

This section presents the finite element discretization of the governing equations presented in Section 2, together with an adaptive remeshing technique. The propagation of wing cracks is complicated, and their trajectories are difficult to achieve by analytical or semianalytical approaches, particularly when multiple fractures interact. In this case, numerical solutions by means of the finite element method (FEM) are a common approach. The finite

element formulation is based on the weak formulation established from the governing equation and states: Find $\mathbf{u} \in V_S$ such that $\forall \mathbf{v} \in V_T$

$$\int_{\Omega} \mathbf{u}^T \mathbf{L}^T \mathbf{D} \mathbf{L} \mathbf{v} d\Omega - \int_{\Gamma_c} \boldsymbol{\sigma} \cdot \mathbf{n} \mathbf{v} d\Gamma = \int_{\Omega} \mathbf{b} \mathbf{v} d\Omega + \int_{\Gamma_N} \bar{\mathbf{f}} \mathbf{v} d\Gamma \quad (17)$$

where V_T and V_S are the test space and the solution space satisfying the inhomogeneous Dirichlet boundary conditions (so-called essential boundary conditions), respectively. V_T and V_S are defined by

$$V_T := \left\{ \mathbf{v} \in H_0^1(\Omega), \mathbf{v}|_{\Gamma_D} = 0 \right\}, \quad V_S := \left\{ \mathbf{v} \in H^1(\Omega), \mathbf{v}|_{\Gamma_D} = \mathbf{u}_0 \right\}, \quad (18)$$

where $H^1(\Omega)$ is the Sobolev space of functions that are square integrable and have a square integrable first derivative. In Eq. (17) \mathbf{L} is the differential operator, and \mathbf{D} is the material matrix modified from \mathbf{C} and defined by

$$\mathbf{L} = \begin{bmatrix} \partial/\partial x & 0 & \partial/\partial y \\ 0 & \partial/\partial y & \partial/\partial x \end{bmatrix}^T \quad (19)$$

$$\mathbf{D} = \frac{E}{1-\nu^2} \begin{bmatrix} 1 & \nu & 0 \\ \nu & 1 & 0 \\ 0 & 0 & \frac{1}{2}(1-\nu) \end{bmatrix}, \text{ for plane stress} \quad (20)$$

$$\mathbf{D} = \frac{E}{(1+\nu)(1-2\nu)} \begin{bmatrix} 1-\nu & \nu & 0 \\ \nu & 1-\nu & 0 \\ 0 & 0 & \frac{1}{2}(1-2\nu) \end{bmatrix}, \text{ for plane strain} \quad (21)$$

3.1. Deformation and contact mechanics

The approximate solution of Eq. (1), denoted by \mathbf{u}^h , can be evaluated by using a subset of the allowable function space $V_h \subset V_S$ composed of piecewise polynomial functions. This requires discretizing the domain Ω into m nonoverlapping finite elements that conform to the fracture geometry, such that

$$\Omega \cong \Omega^h \equiv \bigcup_{e=1}^m \Omega_e \quad (22)$$

In this work, Ω_e are chosen as triangular elements.

The numerical approximation employed on the grid differs between the interior elements that are close to the fracture tip and the interior elements that are not. On elements

that are not connected to the crack tip, the displacement field is approximated as a quadratic function, which is expressed in terms of the displaced values, \mathbf{d}^h , at the three vertices and the midpoints of the three edges such that

$$\mathbf{u} = \begin{Bmatrix} u \\ v \end{Bmatrix} \cong \mathbf{u}^h = \sum_{i=1}^6 \begin{Bmatrix} N_i(\xi, \eta) u_i \\ N_i(\xi, \eta) v_i \end{Bmatrix} = \mathbf{N} \mathbf{d}^h \quad (23)$$

where N_i are the shape functions of a 6-node triangular plane isoparametric element defined by Eq. A(1).

To represent the stress singularity at the fracture tip, quarter-point elements (QPE) (Barsoum, 1977) are employed. Each element around the crack tip, as shown in Fig. 2 (a), is mapped by an 8-node plane isoparametric quadrilateral element, as shown in Fig. 2 (b), so that

$$x = \sum_{i=1}^8 N_i(\xi, \eta) x_i, \quad y = \sum_{i=1}^8 N_i(\xi, \eta) y_i \quad (24)$$

where N_i are the shape functions defined by Eq. A(2). Then, the displacement field is approximated through the displacements at 6 nodes, \mathbf{d}^h , as a quadratic function such that

$$\mathbf{u} = \begin{Bmatrix} u \\ v \end{Bmatrix} \cong \mathbf{u}^h = \sum_{i=1}^6 \begin{Bmatrix} N_i^*(\xi, \eta) u_i \\ N_i^*(\xi, \eta) v_i \end{Bmatrix} = \mathbf{N} \mathbf{d}^h \quad (25)$$

where N_i^* are defined by

$$\begin{cases} N_i^*(\xi, \eta) = N_1 + N_7 + N_8, & \text{if } i = 1, \\ N_i^*(\xi, \eta) = N_i, & \text{otherwise.} \end{cases} \quad (26)$$

By using the approximation given in Eq. (25), the numerical stress is singular at the crack tip, similar to the analytical formula shown in Eq. (9). More details are shown in Appendix A.

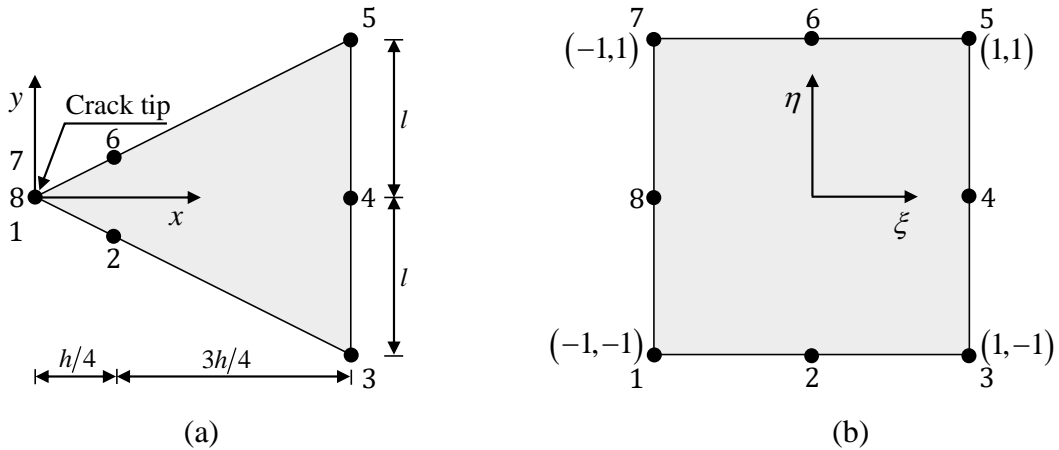


Fig. 2. Definition of the elements around the crack tip (a) and an 8-node plane isoparametric element (b).

By substituting Eqs. (23) and (25) into Eq. (17), the discretized system can be written as

$$\mathbf{K}\mathbf{d}^h = \mathbf{F} = \mathbf{F}_b + \int_{\Gamma_N} \mathbf{N}^T \bar{\mathbf{t}} d\Gamma \quad (27)$$

where \mathbf{K} and \mathbf{F}_b are the global stiffness matrix and global body load vector, respectively, and are obtained by the assembly of the stiffness matrix and body load vector of each element (\mathbf{K}_e and \mathbf{F}_e) that are expressed as

$$\mathbf{K}_e = \int_{\Omega_e} \mathbf{B}^T \mathbf{D} \mathbf{B} d\Omega, \quad \mathbf{F}_e = \int_{\Omega_e} \mathbf{N}^T \mathbf{b} d\Omega \quad (28)$$

where \mathbf{B} is the gradient matrix defined as

$$\mathbf{B} = \mathbf{L} \mathbf{N} \quad (29)$$

The contact mechanics relation defined in Eq. (3) introduces a nonlinearity in the system in that the boundary condition on the fracture depends on whether the fracture is in contact or not. This nonlinearity is treated at each pair of contact points by the active set strategy (Hüeber and Wohlmuth, 2005). The details of the active set algorithm are shown in Fig. 3 and explained as follows:

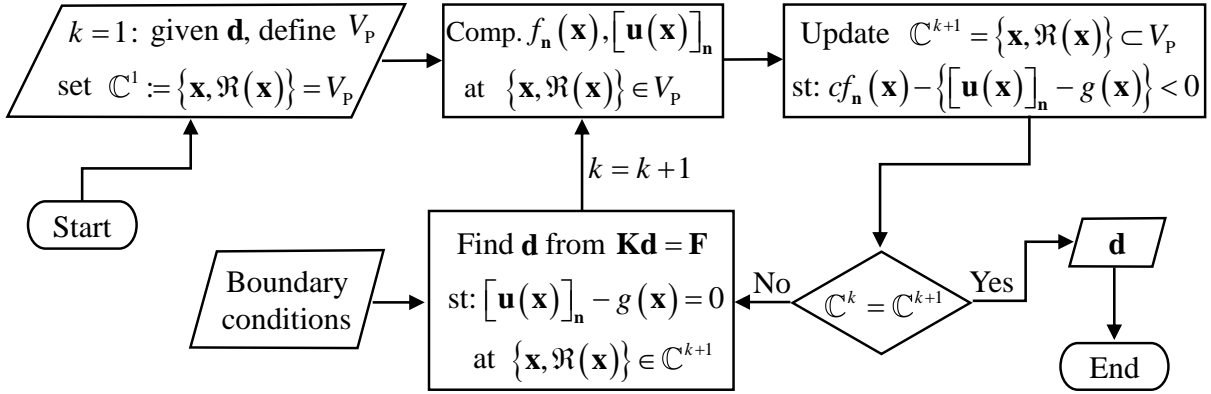


Fig. 3. The numerical solver for the contact mechanics problem.

(1) Set $k = 1$, initialize \mathbf{d} as an initial solution, predict a set of possible contact points V_p and assume the actual contact zone $\mathbb{C}^1 = V_p$. V_p is defined as

$$V_p = \{\mathbf{x}, \mathfrak{R}(\mathbf{x})\}, \quad \mathbf{x} \in \Gamma_C^+ \quad (30)$$

(2) Define the normal displacement jump $[\mathbf{u}(\mathbf{x})]_{\mathbf{n}}$ and normal traction $f_n(\mathbf{x})$ at points $\{\mathbf{x}, \mathfrak{R}(\mathbf{x})\}$ by Eq. (2).

(3) With the current solution, the points $\{\mathbf{x}, \mathfrak{R}(\mathbf{x})\}$ are in contact if the normal displacement jump and normal traction satisfy the following condition:

$$cf_n(\mathbf{x}) - \{[\mathbf{u}(\mathbf{x})]_{\mathbf{n}} - g(\mathbf{x})\} < 0, \quad \mathbf{x} \in \Gamma_c^+ \quad (31)$$

where c is a positive constant depending on the material. If Eq. (31) is satisfied, either $f_n(\mathbf{x}) < 0$, $[\mathbf{u}(\mathbf{x})]_{\mathbf{n}} - g(\mathbf{x}) \geq 0$ or $f_n(\mathbf{x}) = 0$, $[\mathbf{u}(\mathbf{x})]_{\mathbf{n}} - g(\mathbf{x}) > 0$. Therefore, the pair $\{\mathbf{x}, \mathfrak{R}(\mathbf{x})\}$ should be considered as the contact points for the calculation in the next step.

(4) Check if the contact zone at step k , \mathbb{C}^k , is the same as step $k + 1$, \mathbb{C}^{k+1} . If yes then stop, else, the nonpenetration condition $[\mathbf{u}(\mathbf{x})]_{\mathbf{n}} - g(\mathbf{x}) = 0$ at the contact points is counted for the system by using the Lagrangian multiplier, then go to step (2).

3.2. Fracture propagation

The modeling of wing crack propagation is based on two assumptions. First, the wing crack emerges from the tip of the fracture, and second, a crack stops growing whenever its tip reaches a domain boundary or another fracture. That is, we do not consider the fracture propagation that crosses other fractures.

As detailed in Section 2.2, the fracture computation is based on the stress intensity factor evaluation. In this work, we compute SIFs by using the nodal displacement correlation technique (Parks, 1974) in conjunction with QPE (Barsoum, 1976; Henshell and Shaw, 1975) that not only captures the singularity of the stresses but also considerably improves the displacement near the crack tip, resulting in a more accurate computation of the SIFs (Khoei et al., 2008). Through the displacement of the QPE around a crack tip, these SIFs can be calculated as (Chen and Kuang, 1992; Kuang and Chen, 1993)

$$K_{\text{I}} = \frac{E}{6(1+\nu)(1+k)} \sqrt{\frac{2\pi}{h}} [8(v'_b - v'_d) - (v'_c - v'_e)], \quad (32)$$

$$K_{\text{II}} = \frac{E}{6(1+\nu)(1+k)} \sqrt{\frac{2\pi}{h}} [8(u'_b - u'_d) - (u'_c - u'_e)], \quad (33)$$

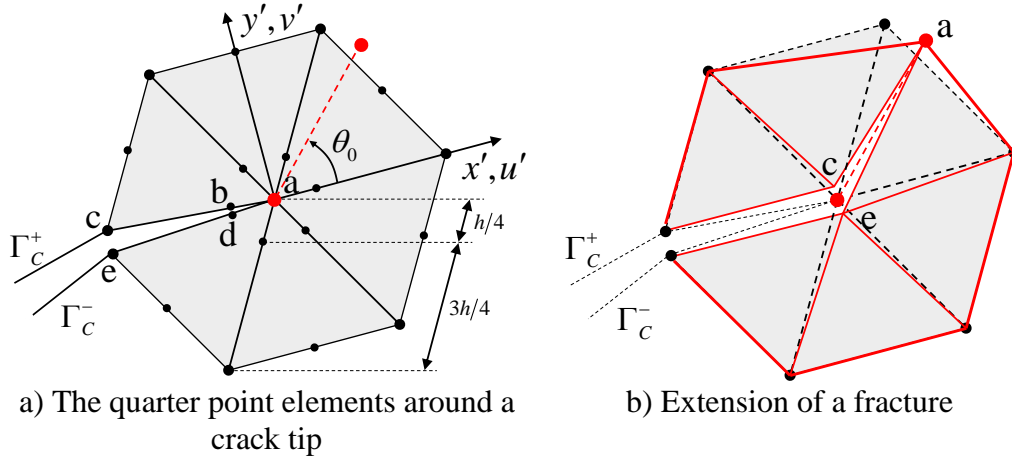


Fig. 4. The quarter point elements around a crack tip and the extension of a fracture.

where $k = (3 - \nu) / (1 + \nu)$ for a plane stress problem and $k = 3 - 4\nu$ for a plane strain problem. As shown in Fig. 4 (a), h is the crack tip rosette radius or size of the element around the crack tip. u' and v' are the local displacements of the nodal points located on the crack in the QPE, in which x' is aligned in the direction of the crack axis.

In the current approach, each time a crack propagates, a new crack tip must be defined by the propagation length L_{adv} and crack initiation angle θ_0 . To ensure the validity of the grid and to reduce the computational cost associated with updates to the grid geometry, a tolerance for geometric mismatch based on the crack tip rosette radius h , $L_{min}^i = 0.4h^i$ is introduced. If $L_{adv}^i < L_{min}^i$, the crack will not be allowed to move, except in the special case when $\theta_0^i = 0$, when the tip position is updated by moving the tip node to a new position. If $L_{adv}^i \geq L_{min}^i$, the crack tip is extended by splitting the previous tip into two new nodes, as shown in Fig. 4 (b). This process also entails that the grid geometry is updated in the vicinity of the crack, as detailed in the next subsection.

3.3. Adaptive remeshing

The accuracy of the numerical simulation depends on the quality of the mesh that is affected by the geometric discretization errors and the gradients of the solution within the individual elements. In this work, we use the adaptive mesh refinement to obtain a solution that satisfies a given mesh discretization error while minimizing the number of elements. The adaptive remeshing (ARM) process involves two techniques: first, mesh refinement based on the error estimator (Zienkiewicz and Zhu, 1987) is used to improve the accuracy of the numerical solution, and second, Laplacian smoothing (Buell and Bush, 1973; Field, 1988) is used to improve the quality of the mesh.

3.3.1 Error estimator and refinements

The error estimator is based on the comparison between the numerical stress computed directly from the computed displacement field and a recovered stress with higher regularity. The numerical stress is directly computed by Eq. (1):

$$\boldsymbol{\sigma}^h = \mathbf{C} : \frac{1}{2} \left[\nabla \mathbf{u}^h + (\nabla \mathbf{u}^h)^\top \right] \quad (34)$$

The quadratic approximation for the displacement renders a numerical stress that is a piecewise linear function on the elements and discontinuous across the interelement boundaries. To recover a globally continuous stress, we first define a nodal stress $\boldsymbol{\sigma}_i^*$ by area-weighted averaging of the elements in the surrounding node:

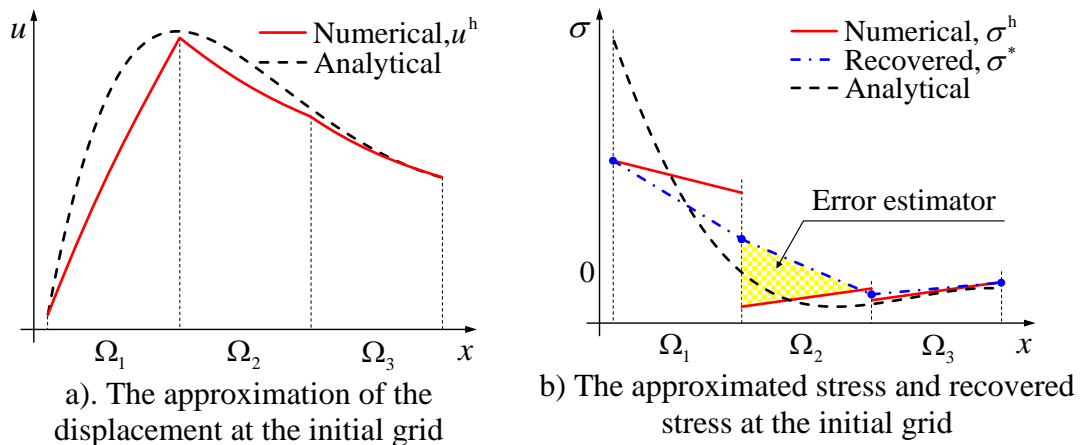
$$\boldsymbol{\sigma}_i^* = \frac{1}{\sum_{i=1}^n A_{\Omega_i}} \sum_{i=1}^n \int_{\Omega_i} \boldsymbol{\sigma}^h d\Omega \quad (35)$$

where A_{Ω_i} is the area of element Ω_i that has node i as a vertex. The recovered stress is then defined by linear interpolation between the stress values $\boldsymbol{\sigma}_i^*$.

The error at each element is estimated by the difference between the numerical and recovered stresses, such as

$$e_{\Omega_i} = \|\boldsymbol{\sigma}^h - \boldsymbol{\sigma}^*\|_{\Omega_i} \quad (36)$$

The refinement is then performed based on a calculated error estimator. The essence of this process is to balance the errors between the elements. This means that the elements in regions of high error are locally refined. This process is repeated until the desired accuracy is obtained.



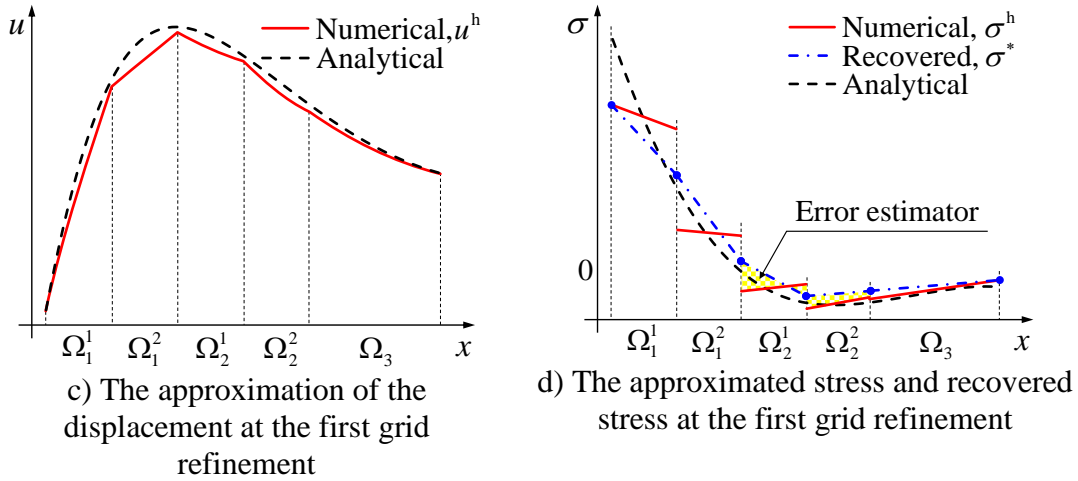


Fig. 5. The procedures for the error estimator and mesh refinement for a one-dimensional problem using a quadratic approximation.

Fig. 5 illustrates the recovery process and mesh refinement in the case of the 1D domain. The refinement with a high estimated error (Ω_1 and Ω_2) increases the accuracy in both the displacement and the stress computations. With the same idea as the 1D, in a 2D problem, the element Ω_i that needs to be refined (Fig. 6 (a)) is divided into four subelements by the connection between the midpoints of the edges (Fig. 6 (b)). Three hanging nodes appear. These nodes are removed by connecting it to an opposite vertex, as shown in Fig. 6 (c).

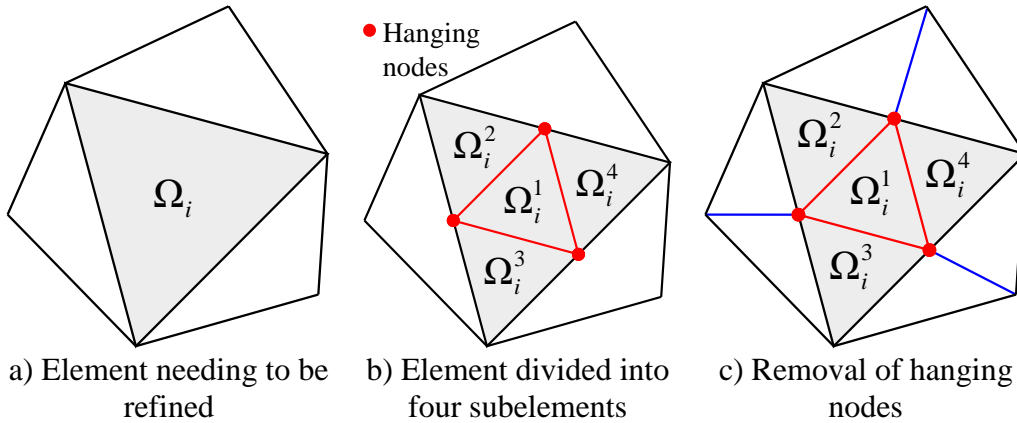


Fig. 6. The refinement processes.

3.3.2 The mesh smoothing process

The mesh refinement process proposed above is local and therefore has a low implementation cost. However, the locality sometimes causes triangles with undesirable properties, such as overlapping elements. We improve the quality of the mesh by using the Laplacian smoothing process that is defined as follows: Let triangles E_i , $i = 1, \dots, n$, share an internal vertex $\mathbf{x}^* = (x^*, y^*)$, and let the remaining vertices of E_i , be $\mathbf{x}_i = (x_i, y_i)$. The node \mathbf{x}^* is updated by the equation

$$\mathbf{x}^* = \frac{1}{n} \sum_{i=1}^M \mathbf{x}_i \quad (37)$$

A precaution is taken to guarantee that the new coordinate assigned to \mathbf{x}^* will define valid triangles. The new coordinate for \mathbf{x}^* is immediately used for all subsequent Laplacian smoothing of other coordinates.

The general algorithm for the fracture propagation simulation in conjunction with the adaptive remeshing and accounting for the fracture contact mechanics is presented in Fig. 7. The item “numerical solver” requires the solution of the contact mechanics problem, as shown in Fig. 3.

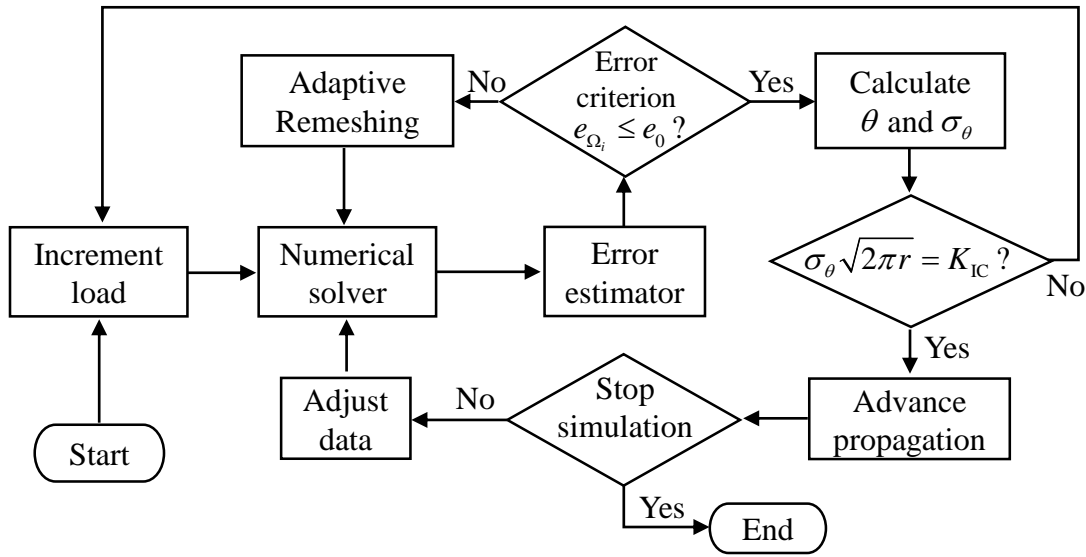


Fig. 7. Processing of the fracture propagation simulation

4. Numerical investigation

In this section, four numerical examples are investigated. The first and second examples are intended for verification and validation purposes, investigating the convergence rates and comparison with the analytical solutions and experimental results. The last two examples are designed to show how the methodology can handle the complex case of shear deformation for a domain with multiple fractures, accounting for wing crack formation as well as fracture contact mechanics.

4.1. Method verification

To evaluate the new approach, we consider a benchmark problem with the propagation of an isolated crack in a medium that undergoes tensile or shear stress. For this problem, the performance of the second order finite element method and quarter point elements (FEM-QPE) with and without adaptive mesh refinement is compared to that of conventional finite elements.

The performance is measured in terms of the accuracy of the strain energy and SIF computation under grid refinement.

The model problem is a thin rectangular plate (length L , width b , and thickness t) including a pre-existing edge fracture, which is subject to tensile (mode I) or shear (mode II) stress as illustrated in Fig. 8. To make a fair comparison, as shown in Fig. 9, the FEM and FEM-QPE use a unique mesh, while the variant of the latter method that includes ARM (FEM-ARM-QPE) uses a multi-size-mesh controlled by the error estimator. The strain energy is given by

$$U(\mathbf{u}) = \frac{1}{2} \int_{\Omega} \boldsymbol{\sigma}^T \boldsymbol{\varepsilon} d\Omega \quad (38)$$

For the plane stress singularity problem, the rate of convergence of the numerical solution is bounded satisfying (Pin and Pian, 1973a)

$$U(\mathbf{u}^h - \mathbf{u}^{\text{exact}}) \leq ch^{2\alpha-2+n} \quad (39)$$

where \mathbf{u}^h and $\mathbf{u}^{\text{exact}}$ denote the solution from the numerical method and the exact solution, and n and α are the spatial dimension of the domain and the singularity degree of solution near the point of singularity, respectively. In the current case, $n = 2$ and $\alpha = 1/2$ (by Eq. (9)); hence, the convergence of the strain energy is linear with h .

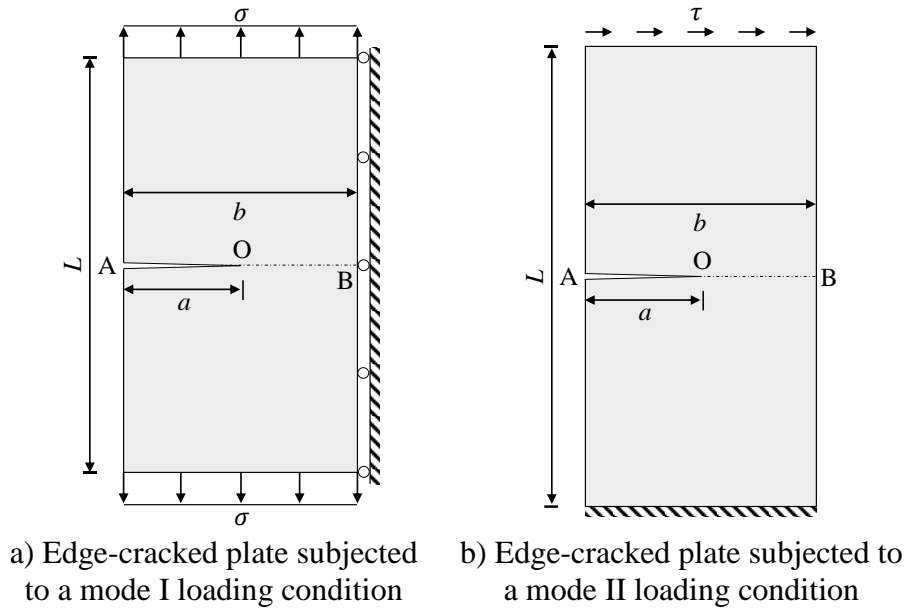


Fig. 8. Plane stress problem considered for the investigation of the convergence of the strain energy and SIFs

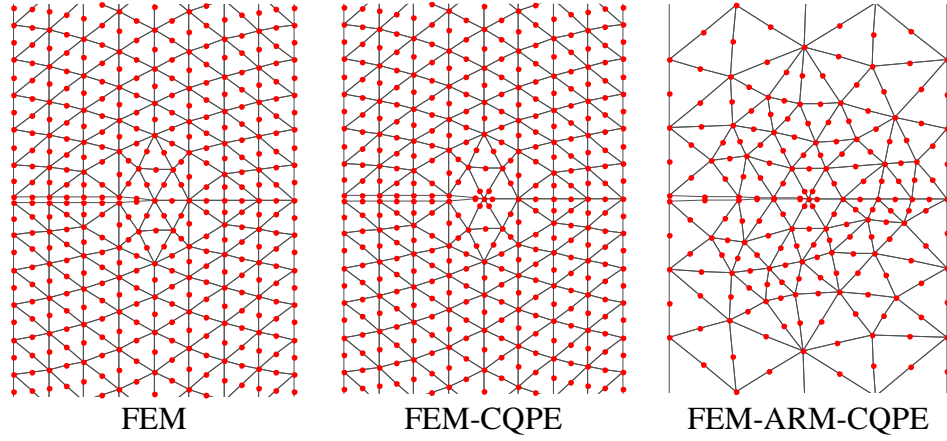
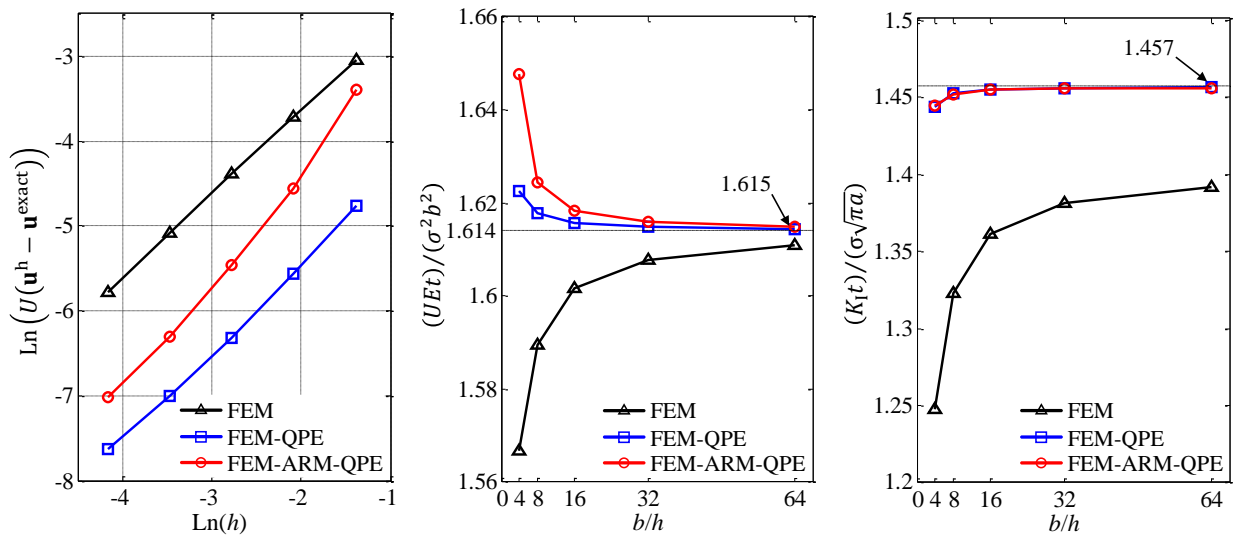


Fig. 9. The discretization with $h = b/8$

For the mode I study, the comparisons of the convergence of the strain energy between the three different methods are shown in Fig. 10 (a, b). A linear convergence rate for the strain energy can be observed, in accordance with Eq. (39) and the conclusions by previous published studies (A. Mirza and D. Olson, 1978; Pin and Pian, 1973b). However, the FEM-QPE is significantly more accurate than the FEM. The convergence rate of the FEM-ARM-QPE is better than that of the FEM, and its accuracy approaches that of the FEM-QPE if the mesh refinement is sufficiently good. The comparison with the analytical solution (Tada et al., 2000) for the stress intensity factor is shown in Fig. 10. (c). The QPEs considerably improve the solution near and ahead of the crack tip and result in a more accurate computation of the SIF. The ARM technique reduces the computational cost while still ensures the accuracy of the computation of the strain energy and stress intensity factor. This is confirmed by Table 1, which shows the total number of degrees of freedom (DOF) and total number of elements for the three methods under grid refinement.



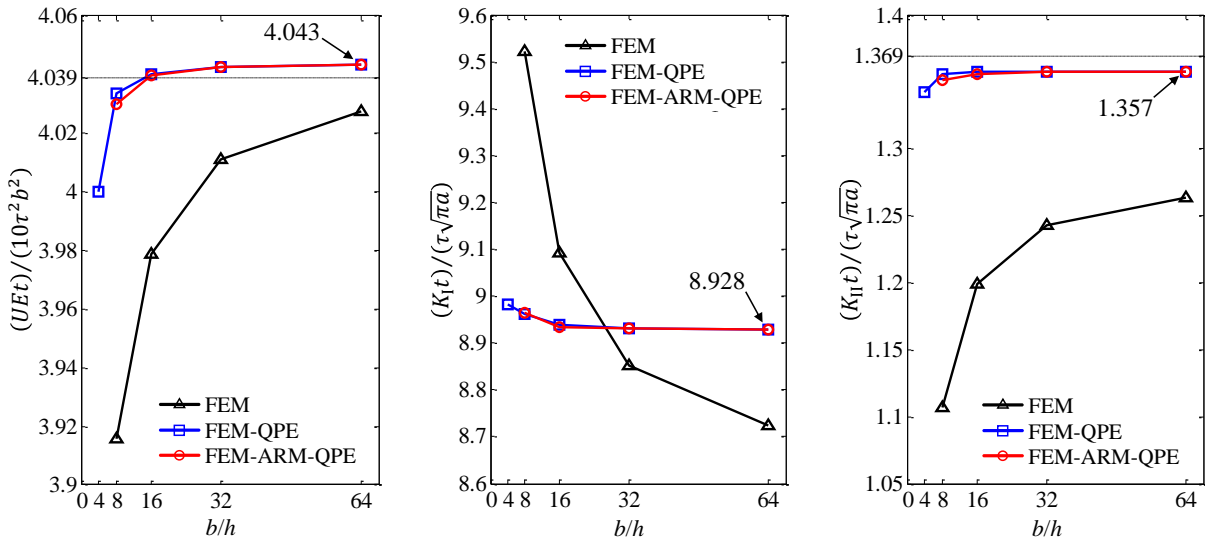
- a) Error in the strain energy for mode I with grid refinement
 $b = 1 \text{ m}, L/b = 2, b/a = 2$
- b) Strain energy for mode I with grid refinement
 $b = 1 \text{ m}, L/b = 2, b/a = 2$
- c) SIF for mode I with grid refinement
 $b = 1 \text{ m}, L \gg b, b/a = 2$

Fig. 10. Convergence study for mode I

Table 1. Comparison between the computational costs of the three methods under grid refinement ($L/b = 2, b/a = 2$).

Computational costs	Method	b/h				
		4	8	16	32	64
DOF	FEM	330	1106	4290	16802	66402
	FEM-QPE	330	1106	4290	16802	66402
	FEM-ARM-QPE	214	678	1454	4970	17742
Total number of elements	FEM	68	248	1016	4088	16376
	FEM-QPE	68	248	1016	4088	16376
	FEM-ARM-QPE	44	152	340	1196	4348

For the mode II study, the reference solutions are obtained by ANSYS for the strain energy and by ABAQUS (Treifi et al., 2008) for K_{II} . As shown in Fig. 11, as in the case of tensile stress, the QPE improves the accuracy of the solutions close to the stress singularity, and the ARM technique preserves the accuracy with fewer degrees of freedom.



- a) Strain energy for mode II with grid refinement
 $b = 1 \text{ m}, L/b = 2, b/a = 2$
- b) SIF for mode I with grid refinement
 $b = 1 \text{ m}, L/b = 2, b/a = 2$
- c) SIF for mode II with grid refinement
 $b = 1 \text{ m}, L/b = 2, b/a = 2$

Fig. 11. Convergence study for mode II

The demonstrated accuracy and efficiency of the FEM-ARM-QPE methodology, shown in previous studies, make it suitable for numerical examples considering more complex geometries in the following section.

4.2. Model validation

To further validate the presented numerical model, FEM-ARM-QPE, the initiation and propagation of wing cracks from the ends of a pre-existing fracture under uniaxial compression loading are investigated. The test case focuses on the accuracy in the computation of the SIFs and fracture propagation paths for a case where both analytical (Atkinson et al., 1982) and experimental (Haeri et al., 2014b) data are available.

The computational domain is a disc-shaped rock specimen containing a central single pre-existing fracture, as shown in Fig. 12. Here, R and t denote the radius and thickness of the disc, and $2a$ is the length of the fracture. The fracture is inclined at an angle φ to the vertical direction at the center of the specimen. The specimen is compressed by two line loads $\mathbf{f}_0 = \{0, f_0\}$ and $-\mathbf{f}_0 = \{0, -f_0\}$ acting parallel to the y -axis. The material parameters are the Young's modulus $E = 15$ GPa, Poisson's ratio $\nu = 0.21$, and fracture toughness $K_{IC} = 2$ MPa·m^{1/2} (Haeri et al., 2014b). On the existing fracture, a no-friction condition is assigned in the tangential direction. For this problem, the analytical solution for the SIFs is given by (Atkinson et al., 1982)

$$\begin{cases} K_I \\ K_{II} \end{cases} = \frac{f_0 \sqrt{a}}{\sqrt{\pi R}} \begin{cases} 1 - 4 \sin^2 \varphi + 4 \sin^2 \varphi (1 - 4 \cos^2 \varphi) \frac{a^2}{R^2} \\ 2 \sin(2\varphi) + \sin(2\varphi) (8 \cos^2 \varphi - 5) \frac{a^2}{R^2} \end{cases} \quad (40)$$

The fracture is a purely mode I fracture for $\varphi = 0^\circ$ and $\varphi = 90^\circ$, while it is a mixed mode fracture for all other angles, with shear effects being most pronounced at $\varphi = 45^\circ$.

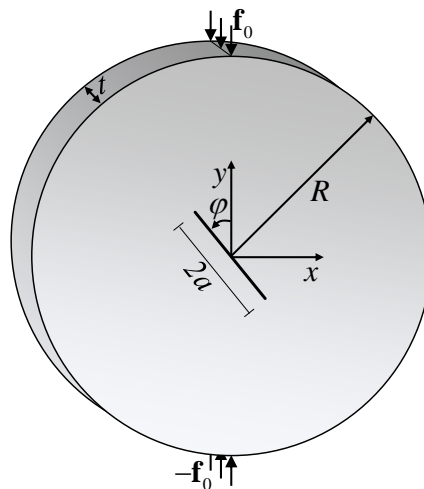


Fig. 12. Geometry of the specimen with a single pre-existing fracture

Numerical, analytical and experimental results for the nondimensional SIFs considering different crack inclination angles are shown in Table 2 and Fig. 13. The computation of the SIFs by the FEM-ARM-QPE model is in good agreement with both the analytical solution (Atkinson et al., 1982) and the experimental data (Haeri et al., 2014b) for various inclination angles of the pre-existing crack.

Fig. 14 shows the computed propagation paths together with the experimental observations (Haeri et al., 2014b) of two wing cracks originating from the tips of the pre-existing fracture. The paths are symmetrically curvilinear and tend to migrate stably and gradually turn in the loading direction. A good agreement between the proposed model and the experiment is recognized in cases where $\varphi = 30^\circ$ and $\varphi = 60^\circ$. For $\varphi = 45^\circ$, the wing cracks obtained by the experiment are asymmetric and visibly different from those computed numerically. We do not consider this a concern for accuracy of the numerical method and note that the simulations consistently predict propagation towards the locations of the point loads, independent of the fracture rotation angle.

Table 2. Comparison of K_I and K_{II} for different crack inclination angles ($a = 5$ mm, $R = 42$ mm).

φ (deg)	$K_I \sqrt{\pi R} / (f_0 \sqrt{a})$			$K_{II} \sqrt{\pi R} / (f_0 \sqrt{a})$		
	Present model	Analytical (Atkinson et al., 1982)	Experimental (Haeri et al., 2014b)	Present model	Analytical (Atkinson et al., 1982)	Experimental (Haeri et al., 2014b)
0	1.0269	1.0	1.0	0.0	0.0	0.0
15	0.7420	0.7323	0.715	1.0069	1.0175	1.017
30	-0.0272	0.0035	-0.016	1.7251	1.7443	1.778
45	-1.0417	-0.9858	-1.014	1.9601	1.9858	2.040
60	-2.0252	-1.9681	-2.054	1.6787	1.6952	1.712
75	-2.7469	-2.6827	-2.701	0.9580	0.9684	0.947
90	-3.0132	-2.9433	-2.948	0.0	0.0	0.0

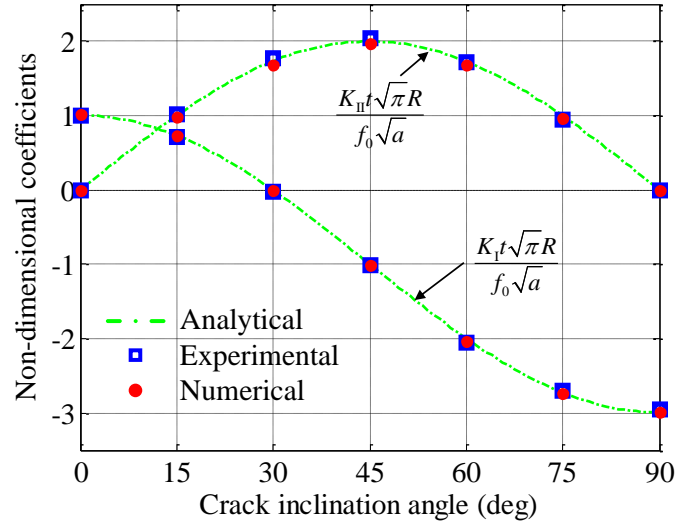


Fig. 13. Variation of nondimensional SIFs with crack inclination angles

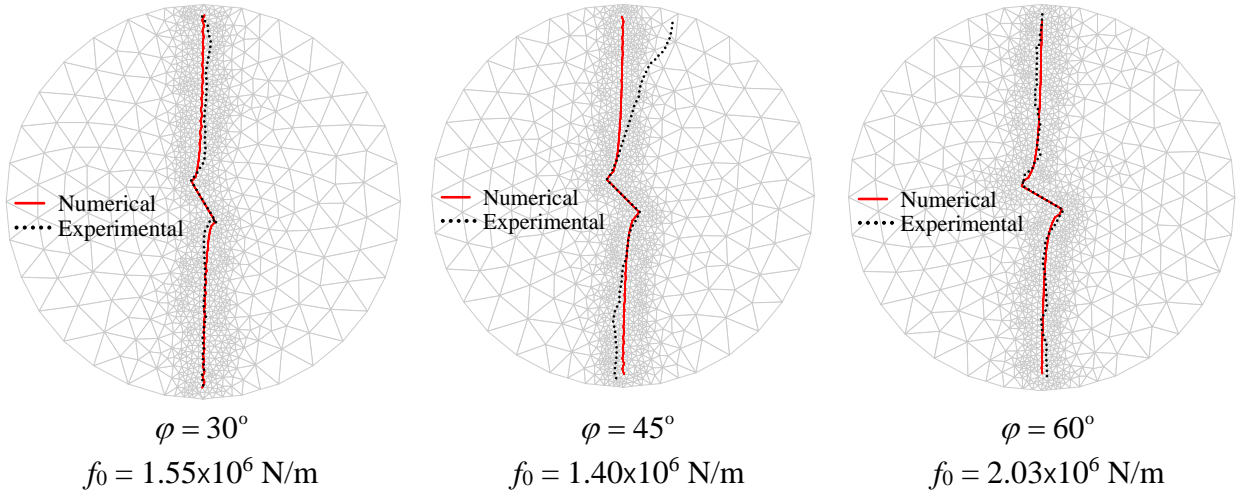


Fig. 14. Comparison of fracture propagation paths between the present model and experiment (Haeri et al., 2014b).

The agreement with the experimental observations in the above examples shows that the mathematical model and the simulation approach proposed in this work are valid for fracture propagation of wing cracks.

4.3. Wing crack propagation due to shearing along a pre-existing fracture

The third example investigates the formation and propagation of wing cracks in a domain with multiple pre-existing fractures, with fracture propagation driven by shearing along one of the fractures. The setup is designed so that the existing fractures will first be linked by newly formed wing cracks, followed by further wing crack formation from the extremities of the newly formed network. The objectives of the example are to analyse the propagation, connection, and final geometry of the generated fracture network. The material parameters are chosen to resemble those of a granite rock mass, with a Young's modulus $E = 70$ GPa,

Poisson's ratio $\nu = 0.21$, mass density $\rho = 2700 \text{ Kg/m}^3$ and fracture toughness $K_{IC} = 1.5 \text{ MPa}\cdot\text{m}^{1/2}$. The gravity is $g = 9.8 \text{ m/s}^2$.

The initial configuration consists of three horizontal parallel natural fractures shown in Fig. 15. The geometrical parameters are $W = 7 \text{ m}$, $D = 6 \text{ m}$, thickness $t = 1 \text{ m}$, $a = 1 \text{ m}$, $b = 0.5 \text{ m}$, and $h_0 = 1 \text{ m}$. There is no opening of the pre-existing fractures. To mimic the subsurface conditions, we assume that this granite rock mass is located at a depth of $H = 1000 \text{ m}$ and subjected to in situ stresses resulting from the weight of the overlying strata (assumed to be granite) approximated by

$$\sigma_x = \frac{\nu}{1-\nu} \rho g H t, \quad \sigma_y = \rho g H t \quad (41)$$

A measurable slip, $\mathbf{u}_0 = \{u_0, 0\}$, is imposed on the middle fracture (fracture 2), mimicking the slip due to the increase in the fluid pressure in the hydraulic shear stimulation of the fractures.

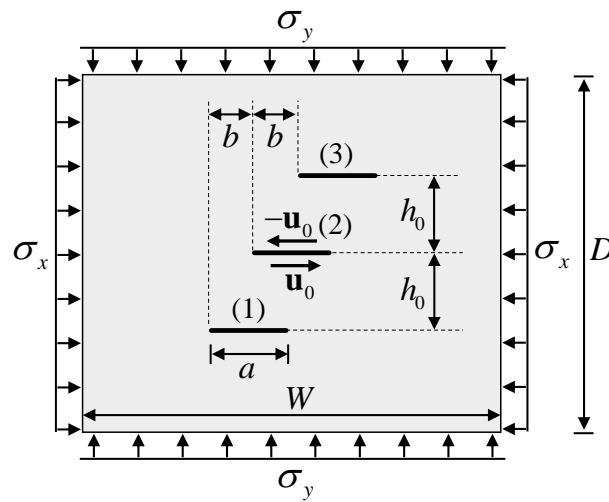


Fig. 15. Geometry of specimens with three pre-existing fractures.

The growth of the wing cracks, the increment of slip and the number of DOFs during the fracture propagation are shown in Fig. 16 and Fig. 17. The number of DOFs is approximately doubled at the end of the simulation. When the pre-existing fracture (2) experiences slip $u_0 = 0.012 \text{ mm}$ in the tangential displacements, wing cracks emerge at its tips. They form an angle of approximately 70 degrees to the main fracture. By increasing the slip until $u_0 = 0.147 \text{ mm}$, wing cracks from fracture (2) gradually turn in the direction perpendicular to the minimum principle stress and connect to fractures (1) and (3). By increasing the slip until $u_0 = 0.3105 \text{ mm}$, two wing cracks newly emerge from fracture (1) and (3) and propagate away.

As shown in Fig. 16, before the wing cracks from fracture (2) reach fractures (1) and (3), the surfaces of pre-existing fractures (1) and (3) are completely in contact. After that, the parts near the connected wing cracks open while the rests are still in contact. The change in the open/closed state of the fractures is caused by the influence of the in situ stresses and the interaction between multiple fractures.

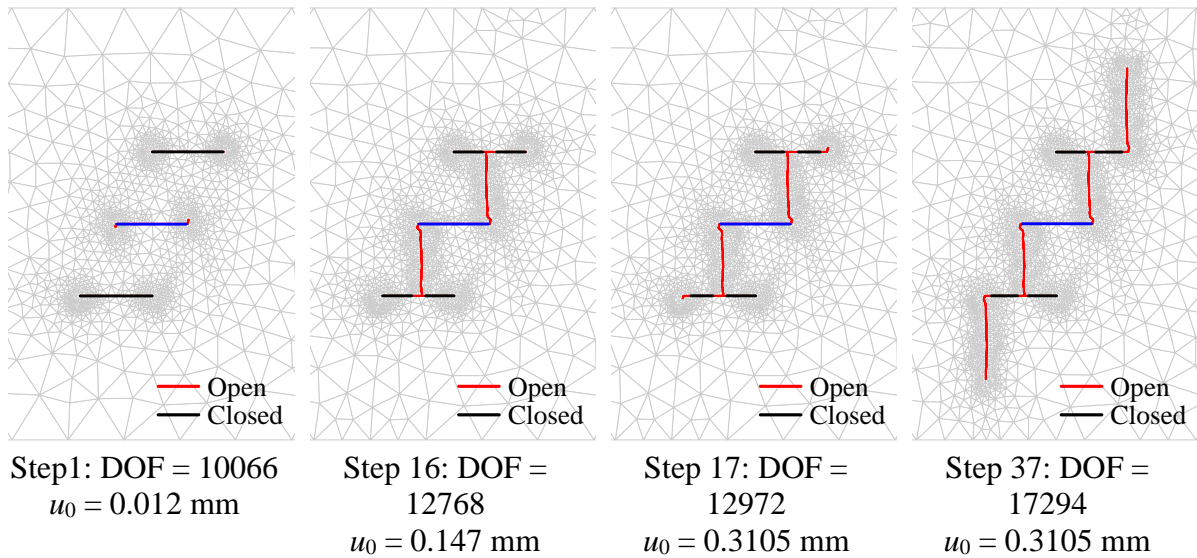


Fig. 16. The trajectories of the wing cracks caused by shear slip at the interfaces of a pre-existing crack.

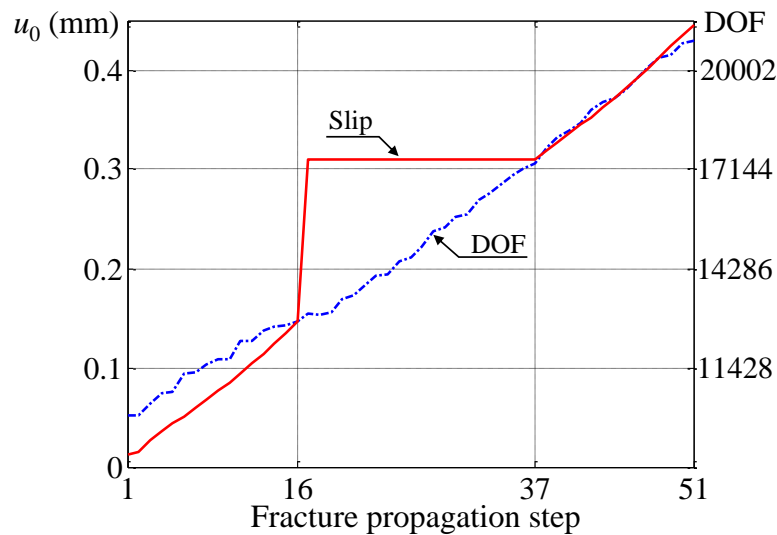


Fig. 17. Increment of slip and DOF during fracture propagation for example 4.3

4.4. Propagation of multiple fractures driven by the shearing boundary conditions

Finally, we consider a more complex case with multiple closed pre-existing fractures arbitrarily appearing in a specimen, as illustrated in Fig. 18. The proposed FEM-AMR-QPE technique is ideally suited to address the complexity of this problem in an efficient and accurate manner.

The size of the specimen is $W = 7$ m, $D = 5$ m, and thickness $t = 1$ m, while the rock parameters are set equal to those in Section 4.3. The boundaries of the specimen are assumed to be subjected to shear forces. The fracture propagation is driven by a gradual increase in the shear forces on the top and bottom boundaries of the domain, while the left and right boundaries are assigned traction free conditions.

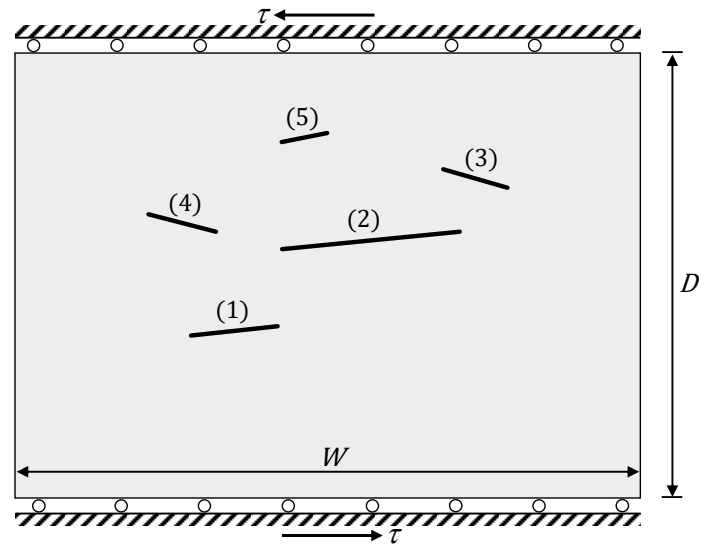
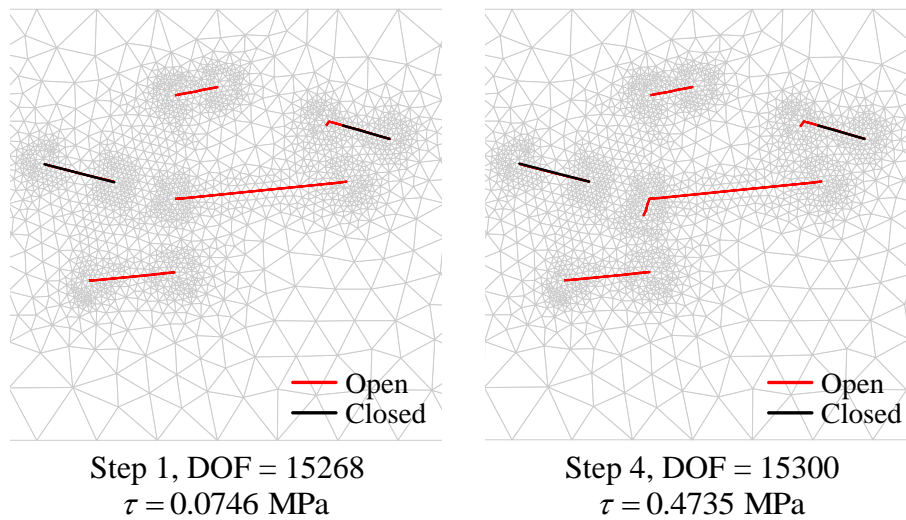


Fig. 18. Geometry of specimens with multiple pre-existing fractures.



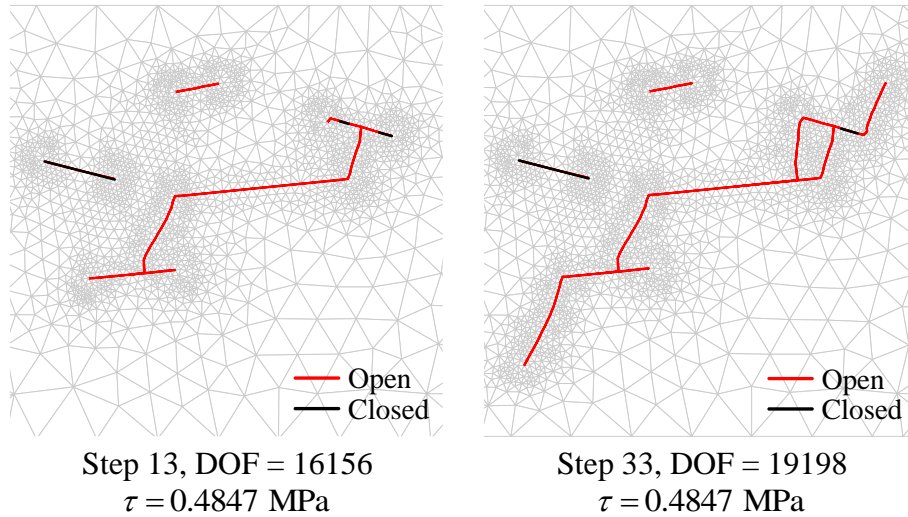


Fig. 19. The trajectories of wing cracks caused by shear slip at the top and bottom sides.

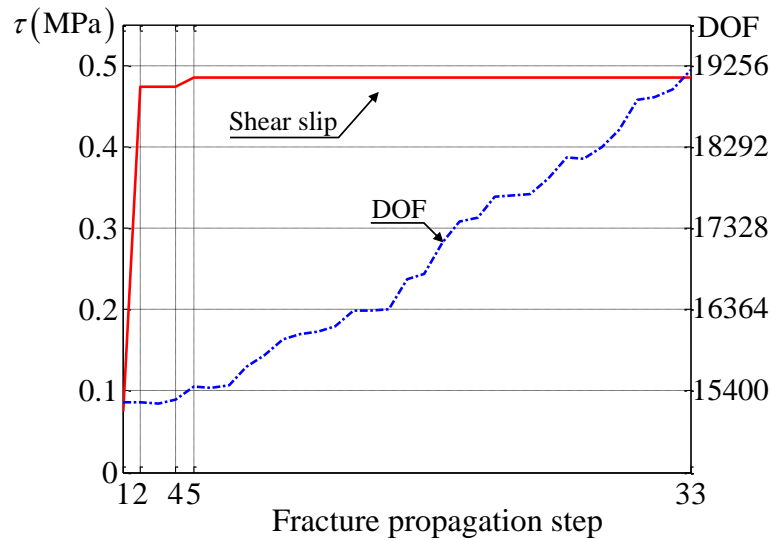


Fig. 20. Increment of slip and DOF during fracture propagation for example 4.4

The propagation trajectory is shown in Fig. 19. The increments of shear slip and the number of DOFs are shown in Fig. 20. The DOFs increased by approximately 30% at the end of simulation. A wing crack first emerges at fracture (3) when the assigned shear stress reached $\tau = 0.0746$ MPa . By increasing the shear stress until $\tau = 0.4735$ MPa , a new wing crack emerges at the end of fracture (2). At $\tau = 0.4847$ MPa , wing cracks emerge at both tips of fracture (2) and propagate in opposite directions; one connects to fracture (3), and the other connects to fracture (1). After that, wing cracks appear at all tips of fractures (1) and (3) and propagate further at different lengths. During shear slip, fractures (4) and (5) do not propagate while the wing cracks propagate in the direction almost 45 degrees with that of shear stress. Fracture (4) is completely closed during the simulation. Fracture (3) is completely closed before wing cracks emerge and is partly closed after that. The remaining fractures are tensile

cracks during propagation. The results clearly show the interaction of the different fractures and the further propagation of wing cracks under shear stress and how the propagation of wing cracks and deformation of the larger fractures prevents wing crack propagation of the smaller fractures.

5. Conclusions

This work presented a numerical model for wing crack initiation and propagation due to shear slip. The governing mathematical model is based on linear elastic fracture mechanics and contact mechanics, along with failure and propagation criteria for multiple mixed-mode fracture propagation. The numerical solution approach is based on a combination of the finite element method combined with quarter point elements to handle the singularity at the fracture tips. The fracture contact mechanics are solved by using the active set strategy. In addition, an adaptive remeshing based on an error estimator and Laplacian smoothing for implementation is utilized for computational efficiency.

Verification and validation studies of the methodology are presented, showing appropriate agreement between the analytical solutions and experimental observations. More complex numerical test cases demonstrated the method's capabilities in investigating the development of wing cracks for situations where multiple fractures interact. The results show how the development of wing cracks interacts with the deformation and propagation of other existing fractures accounting for different fracture contact conditions as well as the overall stress regime.

ACKNOWLEDGEMENTS

This work was funded by the ERiS project, grant #267909, Research Council of Norway.

REFERENCES

- A. Mirza, F., D. Olson, M., 1978. Energy convergence and evaluation of stress intensity factor KI for stress singular problems by mixed finite element method. *Int. J. Fract.* 14, 555–573.
- Anderson, T.L., 2017. *Fracture Mechanics: Fundamentals and Applications*, Fourth Edition. CRC Press.
- Asgian, M.I., 1988. A numerical study of fluid flow in a deformable, naturally fractured reservoir: The influence of pumping rate on reservoir response. 29th U.S. Symp. Rock Mech.
- Atkinson, C., Smelser, R.E., Sanchez, J., 1982. Combined mode fracture via the cracked

- Brazilian disk test. *Int. J. Fract.* 18, 279–291.
- Barsoum, R.S., 1977. Triangular quarter-point elements as elastic and perfectly-plastic crack tip elements. *Int. J. Numer. Methods Eng.* 11, 85–98.
- Bobet, A., Einstein, H.H., 1998. Fracture coalescence in rock-type materials under uniaxial and biaxial compression. *Int. J. Rock Mech. Min. Sci.* 35, 863–888.
- Bryant, E.C., Sun, W., 2018. A mixed-mode phase field fracture model in anisotropic rocks with consistent kinematics. *Comput. Methods Appl. Mech. Eng.* 342, 561–584.
- Buell, W.R., Bush, B.A., 1973. Mesh Generation—A Survey. *J. Eng. Ind.* 95, 332–338.
- Cheng, Q., Wang, X., Ghassemi, A., 2019. Numerical simulation of reservoir stimulation with reference to the Newberry EGS. *Geothermics* 77, 327–343.
- Erdogan, F., Sih, G.C., 1963. On the Crack Extension in Plates Under Plane Loading and Transverse Shear. *J. Basic Eng.* 85, 519–525.
- Field, D.A., 1988. Laplacian smoothing and Delaunay triangulations. *Commun. Appl. Numer. Methods*.
- Gonçalves da Silva, B., Einstein, H., 2013. Modeling of crack initiation, propagation and coalescence in rocks. *Int. J. Fract.* 182, 167–186.
- Haeri, H., Shahriar, K., Fatehi Marji, M., Moarefvand, P., 2014a. Experimental and numerical study of crack propagation and coalescence in pre-cracked rock-like disks. *Int. J. Rock Mech. Min. Sci.* 67, 20–28.
- Haeri, H., Shahriar, K., FatehiMarji, M., Moarefvand, P., 2014b. On the crack propagation analysis of rock like Brazilian disc specimens containing cracks under compressive line loading. *Lat. Am. J. Solids Struct.* 11, 1400–1416.
- Horii, H., Nemat-Nasser, S., 1985. Compression-induced microcrack growth in brittle solids: Axial splitting and shear failure. *J. Geophys. Res. Solid Earth* 90, 3105–3125.
- Hüeber, S., Wohlmuth, B., 2005. A primal–dual active set strategy for non-linear multibody contact problems. *Comput. Methods Appl. Mech. Eng.* 194, 3147–3166.
- Ingraffea, A.R., Heuze, F.E., 1980. Finite element models for rock fracture mechanics. *Int. J. Numer. Anal. Methods Geomech.* 4, 25–43.
- Ingraffea, A.R., Manu, C., 1980. Stress-intensity factor computation in three dimensions with

- quarter-point elements. *Int. J. Numer. Methods Eng.* 15, 1427–1445.
- Jung, R., 2013. EGS — Goodbye or Back to the Future, in: *Effective and Sustainable Hydraulic Fracturing*. InTech, pp. 95–121.
- Kamali, A., Ghassemi, A., 2018. Analysis of injection-induced shear slip and fracture propagation in geothermal reservoir stimulation. *Geothermics* 76, 93–105.
- McClure, M.W., Horne, R.N., 2014. An investigation of stimulation mechanisms in Enhanced Geothermal Systems. *Int. J. Rock Mech. Min. Sci.* 72, 242–260.
- Norbeck, J.H., McClure, M.W., Horne, R.N., 2018. Field observations at the Fenton Hill enhanced geothermal system test site support mixed-mechanism stimulation. *Geothermics* 74, 135–149.
- Oden, J.T., Pires, E.B., 1983. Nonlocal and Nonlinear Friction Laws and Variational Principles for Contact Problems in Elasticity. *J. Appl. Mech.* 50, 67–76.
- Paluszny, A., Matthäi, S.K., 2009. Numerical modeling of discrete multi-crack growth applied to pattern formation in geological brittle media. *Int. J. Solids Struct.* 46, 3383–3397.
- Paris, P., Erdogan, F., 1963. A Critical Analysis of Crack Propagation Laws. *J. Fluids Eng.* 85, 528–533.
- Pin, T., Pian, T.H.H., 1973a. On the convergence of the finite element method for problems with singularity. *Int. J. Solids Struct.* 9, 313–321.
- Pin, T., Pian, T.H.H., 1973b. On the convergence of the finite element method for problems with singularity. *Int. J. Solids Struct.* 9, 313–321.
- Renshaw, C.E., Pollard, D.D., 1994. Numerical simulation of fracture set formation: A fracture mechanics model consistent with experimental observations. *J. Geophys. Res. Solid Earth* 99, 9359–9372.
- Sharafisafa, M., Nazem, M., 2014. Application of the distinct element method and the extended finite element method in modelling cracks and coalescence in brittle materials. *Comput. Mater. Sci.* 91, 102–121.
- Tada, H., Paris, P.C., Irwin, G.R., 2000. *The stress analysis of cracks handbook*. ASME Press, Norwood Mass.
- Treifi, M., Olutunde Oyadiji, S., Tsang, D.K.L., 2008. Computations of modes I and II stress intensity factors of sharp notched plates under in-plane shear and bending loading by the

- fractal-like finite element method. *Int. J. Solids Struct.* 45, 6468–6484.
- Ueber, S., Stadler, G., Wohlmuth, B., 2008. A Primal-Dual Active Set Algorithm for Three-Dimensional Contact Problems with Coulomb Friction. *SIAM J. Sci. Comput.* 30.
- Wong, L.N.Y., Einstein, H.H., 2009. Systematic evaluation of cracking behavior in specimens containing single flaws under uniaxial compression. *Int. J. Rock Mech. Min. Sci.* 46, 239–249.
- Zhang, X., Sloan, S., Vignes, C., Sheng, D., 2017. A modification of the phase-field model for mixed mode crack propagation in rock-like materials. *Comput. Methods Appl. Mech. Eng.* 322, 123–136.
- Zienkiewicz, O.C., Zhu, J.Z., 1987. A simple error estimator and adaptive procedure for practical engineering analysis. *Int. J. Numer. Methods Eng.* 24, 337–357.

APPENDIX A

- The 6-node triangular shape functions are defined by

$$N_i(\xi, \eta) = (1 - \xi - \eta)(1 - \xi_i - \eta_i) \left[16(\xi\xi_i + \eta\eta_i) + (1 - 2\xi - 2\eta)(1 - 2\xi_i - 2\eta_i) \right] \\ + \xi\xi_i(2\xi - 1)(2\xi_i - 1) + 16\xi\eta\xi_i\eta_i + \eta\eta_i(2\eta - 1)(2\eta_i - 1) \quad \text{A(1)}$$

- The 8-node quadrilateral shape functions are defined by

$$N_i(\xi, \eta) = \frac{\xi_i^2 \eta_i^2}{4} \left[(1 + \xi\xi_i)(1 + \eta\eta_i) - (1 - \xi^2)(1 + \eta\eta_i) - (1 + \xi\xi_i)(1 - \eta^2) \right] \\ + \frac{\eta_i^2}{2}(1 - \xi_i)(1 - \xi^2)(1 + \eta\eta_i) + \frac{\xi_i^2}{2}(1 - \eta_i^2)(1 + \xi\xi_i)(1 - \eta^2) \quad \text{A(2)}$$

- The details of the QPE formulation.

Substituting specific coordinates of 6 nodes (x_i, y_i) as shown in Fig. 2. Definition of the elements around the crack tip (a) and an 8-node plane isoparametric element (b).

(a) into Eq. (24) gives

$$x = \frac{h}{4}(1 + \xi)^2, \quad y = \frac{l}{4}(1 + \xi)^2 \eta \quad \text{A(3)}$$

By assuming r is the distance from point (x, y) to the crack tip gives

$$r = \sqrt{x^2 + y^2} \Rightarrow (1 + \xi) = \sqrt{r} A_0(h, l, \eta) \quad \text{A(4)}$$

The Jacobian of the transformation [\mathbf{J}] is given by

$$[\mathbf{J}] = \begin{bmatrix} \partial x / \partial \xi & \partial y / \partial \xi \\ \partial x / \partial \eta & \partial y / \partial \eta \end{bmatrix} = \frac{1}{4} \begin{bmatrix} 2h(1 + \xi) & 2l\eta(1 + \xi) \\ 0 & l(1 + \xi)^2 \end{bmatrix} \quad \text{A(5)}$$

Taking the derivatives both sides of Eq. (25) gives

$$\left\{ \frac{\partial \mathbf{u}^h}{\partial x} \quad \frac{\partial \mathbf{u}^h}{\partial y} \right\}^T = [\mathbf{J}]^{-1} \left\{ \frac{\partial \mathbf{N}}{\partial \xi} \quad \frac{\partial \mathbf{N}}{\partial \eta} \right\}^T \mathbf{d}^h \quad \text{A(6)}$$

The derivatives of the displacement can be explicitly written in the form

$$\frac{\partial u^h}{\partial x} = \frac{1}{(\xi + 1)} A_1(h, u_i, \eta) + A_2(h, u_i), \quad \frac{\partial v^h}{\partial x} = \frac{1}{(\xi + 1)} A_1(h, v_i, \eta) + A_2(h, v_i) \\ \frac{\partial u^h}{\partial y} = \frac{1}{(\xi + 1)} B_1(l, u_i, \eta) + B_2(l, u_i), \quad \frac{\partial v^h}{\partial y} = \frac{1}{(\xi + 1)} B_1(l, v_i, \eta) + B_2(l, v_i) \quad \text{A(7)}$$

By combining Eq. (1), Eq. A(4) and Eq. A(7), the stress components from the numerical method are defined by

$$\begin{Bmatrix} \sigma_x^h \\ \sigma_y^h \\ \tau_{xy}^h \end{Bmatrix} = \frac{1}{\sqrt{r}A_0(h,l,\eta)} \mathbf{D} \begin{Bmatrix} A_1(h,u_i,\eta) + A_2(h,u_i) \\ B_1(l,v_i,\eta) + B_2(l,v_i) \\ A_1(h,v_i,\eta) + A_2(h,v_i) + B_1(l,u_i,\eta) + B_2(l,u_i) \end{Bmatrix} \quad \text{A(8)}$$

where A_i and B_i are defined by

$$A_0(h,l,\eta) = 2(h^2 + l^2\eta^2)^{-\frac{1}{4}} \quad \text{A(9)}$$

$$A_1(h,u_i,\eta) = \frac{1}{h} \begin{bmatrix} 3u_1 + 2(\eta+1)u_2 - (3\eta^2 + \eta + 2)u_3 \\ + (3\eta^2 + 1)u_4 - (3\eta^2 - \eta + 2)u_5 - 2(\eta-1)u_6 \end{bmatrix} \quad \text{A(10)}$$

$$A_2(h,u_i) = \frac{1}{h} (2u_1 - 2u_2 + u_3 + u_5 - 2u_6) \quad \text{A(11)}$$

$$B_1(l,u_i,\eta) = \frac{1}{l} [-4u_2 + 2(\eta+1)u_3 - 4\eta u_4 + (2\eta-1)u_5 + 4u_6] \quad \text{A(12)}$$

$$B_2(l,u_i) = \frac{1}{l} (2u_2 - u_3 + u_5 - 2u_6) \quad \text{A(13)}$$

It is clear that as $r \rightarrow 0$ (which means $\xi \rightarrow 0$ and/or $\eta \rightarrow 0$), the terms A_i and B_i become constants. Therefore, the numerical stresses in Eq. A(8) tend to $O(1/\sqrt{r})$.